High-resolution attosecond imaging of an atomic electron wave function in momentum space

Takashi Nakajima,[1,*] Tasuku Shinoda,[1,*] D. M. Villeneuve,[2] and Hiromichi Niikura[1,†]
[1]*Department of Applied Physics, Waseda University, 3-4-1 Okubo Shinjyuku, Tokyo 169-8555, Japan*
[2]*Joint Attosecond Science Laboratory, National Research Council and University of Ottawa, 100 Sussex Drive, Ottawa, Ontario, Canada, K1A0R6*

(Received 20 September 2022; accepted 2 December 2022; published 23 December 2022)

An electron wave function is characterized by the phase and amplitude distributions over position or momentum space. Recent attosecond technologies allow us to obtain the phase information of photoelectrons using interference between several optical transition pathways. We demonstrate that by employing a two-path photoionization interference process, the complex wave function of the photoelectron is fully mapped in two-dimensional momentum space. We ionize neon gas by an extreme ultraviolet (XUV) attosecond pulse train consisting of both odd and even harmonics in the presence of an infrared (IR) laser field. By controlling the generation process of the attosecond pulse train, we isolate two ionization pathways for interfering with the photoelectrons: one is the two-photon ionization process due to the odd harmonic excitation with one IR photon absorption, and the other is the one-photon ionization by an even harmonic. We record the photoelectron momentum distributions via velocity map imaging as a function of the XUV and IR delay. Using three different experimental conditions, we show that the detailed structure of the amplitude and phase distributions of photoelectrons can be resolved in the two-dimensional momentum space within the bandwidth determined by the attosecond XUV pulse. We separate the measured photoelectron wave function into those produced by each ionization pathway. Our method will be applicable to more complex molecules.

DOI: 10.1103/PhysRevA.106.063513

I. INTRODUCTION

Quantum interference is based on the wave nature of particles [1–3]. The wave nature of electrons is characterized by both phase and amplitude, described by a *complex* wave function. Recent attosecond experiments have provided methods to measure the phase and dynamics of electrons in atoms, molecules, and solids [4–20]. In the attosecond electron recollision approach, the phase and amplitude of a bound state electron wave function or a molecular orbital can be retrieved from the interference between the bound state and recolliding electron wave packets [8–12]. In the multiphoton ionization approach, a probe consisting of an extreme ultraviolet (XUV) train of attosecond pulses in the presence of an infrared (IR) laser field produces two or more photoelectron wave packets interfering in the ionization continuum. From the interference pattern, the phase information of the photoelectron is obtained [13–20].

In this study, we introduce a two-path interference scheme using an attosecond pulse train to obtain a phase and amplitude distribution of photoelectrons in a momentum space. We generate a train of attosecond pulses by focusing an intense IR pulse and its second harmonic into a gas jet. The spectrum of the attosecond pulse train consists of a series of both odd ($2n+1$, n is integer) and even ($2n$) harmonics of the fundamental IR photon energy [19–21]. By controlling the generation process of high harmonics, we isolate two ionization pathways that cause photoelectron interference in the ionization continuum. One pathway is the two-photon ionization by the $(2n-1)$ harmonic excitation plus one IR photon absorption, and the other is the direct ionization by the $(2n)$ harmonic. We ionize neon gas by the XUV and IR pulses, and record the velocity map imaging (VMI) of photoelectrons as a function of the delay between the XUV and the IR pulse. In VMI, the photoelectron momentum distribution is projected onto a two-dimensional plane (k_x, k_y). At every momentum, we fit the modulation of the photoelectron signal intensity as a function of the XUV-IR delay with cosine functions to obtain the phases and amplitudes. From the fitted phase and amplitude distributions, we generate a complex "mapping" wave function, $\Psi(k_x, k_y)$, which is the product of the wave functions generated by the two pathways. Using three different experimental conditions, we show that the mapping wave function is sensitive to small changes of the phase and amplitude. Furthermore, we disentangle the mapping function into the wave function produced by each ionization pathway using partial wave analysis.

Our approach has advantages over previous interference experiments using an attosecond pulse train. The method referred to as the reconstruction of attosecond beating by interference of two-photon transitions (RABBIT) uses two-path interference between the odd harmonics with one IR photon absorption or emission, $(2n+1)$ – IR and $(2n-1)+$ IR [13,14]. In this case, since the photoelectron wave packet

*These authors contributed equally to this work.
†address:niikura@waseda.jp

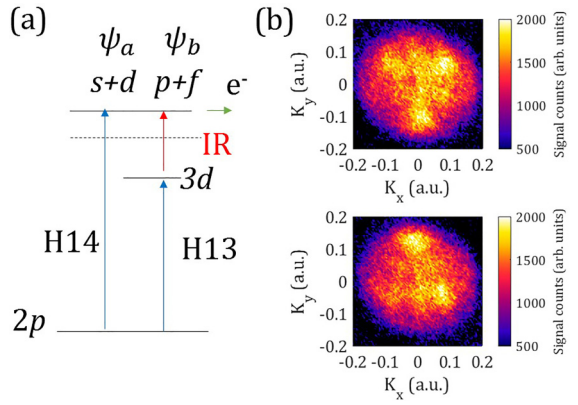

FIG. 1. (a) A schematic energy diagram of the two-path interference photoionization process. Harmonic 14 (H14) produces ψ_a which is a coherent sum of s and d waves. Likewise, harmonic 13 (H13) with one IR photon absorption produces the wave packet ψ_b which is a coherent sum of p and f waves. (b) The measured VMI images at two delays separated by $T_0/2 \sim 1.32$ fs.

produced by one pathway has the same parity as that produced by the other pathway, decomposition of the interfering electron wave packet into the individual wave packet produced by either pathway is difficult. Recently, using three-path interference of photoelectrons produced by the process $(2n+1)$–IR, $2n$, and $(2n-1)$ + IR, the photoelectron wave packet was completely characterized to obtain the phases and amplitudes of all photoelectron angular momentum components [19]. By using two-dimensional attosecond delay measurements, the atomic phase of each partial wave was disentangled from the spectral phase [20]. However, since the global fitting used for the determination of a number of parameters requires sufficient photoelectron signal intensity, these analyses were performed only at a certain averaged radial momentum k_r. In our present study, by limiting the interfering pathways into two, we can directly map the phase difference between the two wave packets produced by the $(2n-1)$ + IR and $(2n)$ ionization pathways. In addition, since the partial wave analysis becomes simpler than the case of three-path interference, the phases and amplitudes of the photoelectron angular momentum components are obtained in a range of k_r to visualize the complex wave function in the ionization continuum.

In general, the energy resolution of a photoelectron spectrum is mainly determined by the bandwidth of the light source. For the attosecond pulse train, increasing the number of single attosecond pulses in the train decreases the bandwidth [7]. In our method, coherent overlap between the photoelectron wave packets with different parities can resolve the detailed structure of the wave packets with a momentum resolution less than 0.02 atomic unit (a.u.), or a kinetic energy resolution of ~0.026 eV, which is much smaller than the bandwidth of the attosecond pulse trains used in this experiment.

Figure 1(a) shows a schematic diagram of the ionization pathways originating from the $2p$ state for a target gas of neon. In the presence of the IR field, harmonic 13 (H13), which is nearly resonant with the $3d$ Rydberg states, produces the f (angular momentum quantum number $\ell = 3$) and p waves ($\ell = 1$) in the ionization continuum. By adjusting the photon energy of the XUV harmonics and the IR intensity, the energy levels with magnetic quantum number $m_\ell = 0$ are preferentially selected [22]. One-photon ionization by harmonic 14 (H14) produces ψ_a which consists of the s ($\ell = 0$) and the d waves ($\ell = 2$), while the two-photon process of H13+IR produces ψ_b consisting of f and p waves. Changing the delay between the XUV and IR pulses changes the interference between ψ_a and ψ_b, and thus the photoelectron wave packet. We choose three experimental conditions with slightly different IR intensities and the photon energies of harmonics. Theoretical study suggests that the momentum distribution of ψ_b produced from the field-modified $3d$ state is sensitive to the small changes in these laser parameters [22]. We show how the phase and amplitude of the f and p waves in ψ_b vary with the photon energy of high harmonics and the IR intensity.

II. EXPERIMENTAL SETUP

Figure 2 illustrates the experimental setup. A dual-stage, multipass amplifier system (Komodo-Dragon, KMLabs) generates 1 kHz, 35 fs, ~790 nm infrared (ω) laser pulses. The beam is split vertically into two half beams that we call A and B. Beam A is delayed by a 1 mm thick D-shaped fused silica plate FS1. A BBO crystal generates the second harmonic (2ω) of both beams; a calcite plate "Ca" and a dual-wavelength waveplate WP2 make the two colors coincident in time in gas jet, "Jet1," and with horizontal polarization. Rotation of the calcite plate, Ca, controls the precise $\omega - 2\omega$ delay. Both beams are focused into a krypton gas emitted from a pulsed gas jet, Jet1, in a vacuum chamber. High harmonics are generated predominantly by beam A. Due to the presence of the second harmonic, both odd and even harmonic orders of 790 nm are produced. In order to make a sharp cutoff in the high-harmonic spectra, a relatively intense 2ω field was used. Wavelength selectivity is achieved by reflection from a set of mirrors, shown in the inset of Fig. 2. The IR field in beam A is removed by Brewster-angle reflection from two silicon mirrors, while the IR in beam B is reflected from the aluminum coating on half of the silicon face. The XUV is removed from beam B by a 1 mm thickness D-shaped fused silica plate FS2, which also brings the IR field in beam B into synchrony with the XUV in beam A (previously delayed by FS1). The IR XUV delay is controlled by rotating FS2. The second harmonic in beam A is also removed by nearly Brewster-angle reflection from the two silicon mirrors, and the second harmonic in beam B is temporally separated from the IR field by FS2. Thus, only the IR field in beam B is temporally overlapped with the XUV in beam A at the ionization region in VMI. Both beams A and B are focused by a 270 mm focal-length toroidal mirror (ARW optical corporation) into the ionization region. A neon gas is introduced by a pulsed gas jet, "Jet2," into the VMI. The XUV from beam A ionizes the neon gas in the presence of the IR field from beam B. The resulting photoelectrons are accelerated upwards in the VMI and recorded by a microchannel plate detector. The transmitted XUV pulse is dispersed by a flat-field grating and the spectrum is imaged onto a microchannel plate. For the fitting of the measured data (see next section), we utilize a MATLAB (MathWorks, Inc.) least-squares fitting function.

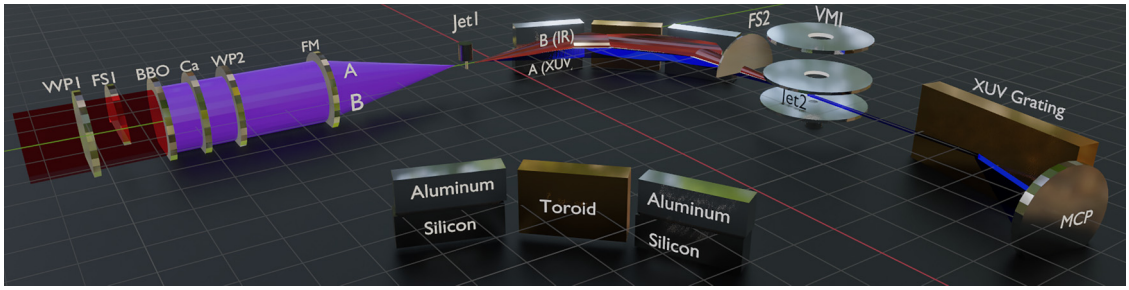

FIG. 2. Schematic diagram of the experimental arrangement. A detailed explanation is in the main text. WP1 = half-wave plate for 790 nm to make the polarization vertical. FS1 = D-shaped fused silica plate to delay the top half, called beam A. BBO = beta barium borate crystal that generates the second harmonic of the 790 nm pulse. Ca = birefringent calcite plate to compensate and control the $\omega - 2\omega$ delay. WP2 rotates the vertical polarization of the ω to horizontal while leaving the 2ω horizontal. FM = focusing mirror (shown as a lens for clarity) focuses the beams into krypton gas jet "Jet1" in the vacuum chamber. A set of mirrors (inset) removes the IR from beam A and focuses both beams into a velocity map imaging spectrometer (VMI) where neon gas is photoionized by the XUV. The neon gas is introduced by "Jet2" in the VMI. The XUV spectrum is recorded by a flat-field grating and MCP detector.

III. EXPERIMENTAL RESULTS AND ANALYSIS

A. High-harmonic spectra for three different conditions

Figure 3 plots the high-harmonic spectra of the XUV pulse as a function of the $\omega - 2\omega$ delay. The measurements and analysis were performed under three experimental conditions, Figs. 3(a)–3(c). The photon energy of high harmonics was tuned by changing the compressor grating position slightly [22]. The intensity of the spectrum is modulated with a half optical period of the 2ω laser field. The 2ω intensity is relatively high compared to the previously performed experiments [19,20], approximately 1% of the IR intensity. We have two independently controllable attosecond delays, the XUV IR delay and the $\omega - 2\omega$ delay [20]. We fix the $\omega - 2\omega$ delay and record the VMI images as a function of the XUV IR delay, τ. Figure 3(d) plots the high-harmonic spectra used for the XUV IR delay dependence measurements. In all three cases, the intensity of H15 is much smaller than that of H13, ensuring that the two-path interference between H13 and H14 is the dominant process.

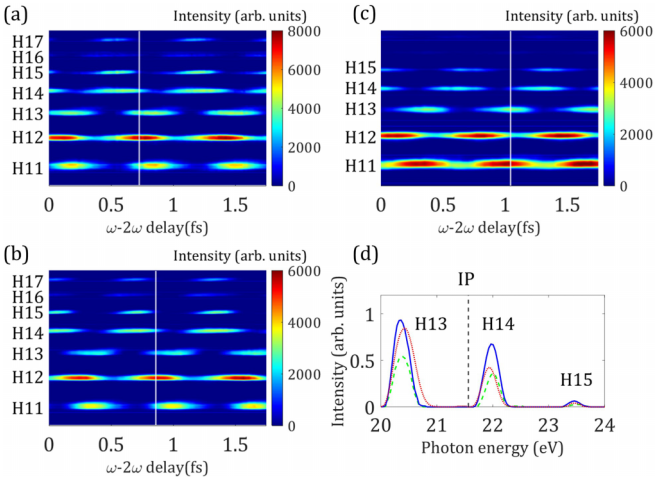

FIG. 3. (a–c) The high-harmonic spectra for three different experimental conditions as a function of the $\omega - 2\omega$ delay. The white line indicates the $\omega - 2\omega$ delay selected for the XUV IR delay dependence measurements, and the spectra are plotted in (d). The blue, green (dashed), red (dotted) curves in (d) correspond to the spectra for (a–c). The zero delay is chosen arbitrarily. The black dotted line in (d) indicates the field-free ionization potential (IP) for neon.

B. Mapping wave functions

Figure 1(b) shows the VMI images recorded at two different XUV IR delays, separated by half of the fundamental laser period, $T_0/2 = \sim 1.32$ fs, corresponding to the high-harmonic spectrum shown as the blue curve in Fig. 3(d). The angular distribution inverts when the delay changes by $T_0/2$. The polarization axis of the XUV and IR pulses is approximately vertical in the figure and parallel to the y axis. The propagation direction of the laser pulses is parallel to the x axis.

In the two-path interference model, the signal intensity of photoelectrons with a certain momentum $\boldsymbol{k}$ is modulated as a function of the delay τ between the XUV and IR pulses, and is given by

$$S(\tau, \boldsymbol{k}) = |\psi_a + \psi_b e^{-i\omega\tau}|^2, \tag{1}$$

where ω is the angular frequency of the fundamental IR pulse, and ψ_a and ψ_b are the wave functions produced by H14 and by H13+IR, respectively, as shown in Fig. 1(a). Writing $\psi_a = |\psi_a|e^{i\varphi_a}$ and $\psi_b = |\psi_b|e^{i\varphi_b}$, $S(\tau)$ is given by

$$S(\tau, \boldsymbol{k}) = |\psi_a|^2 + |\psi_b|^2 + 2|\psi_a||\psi_b|\cos[\omega\tau + (\varphi_a - \varphi_b)]. \tag{2}$$

The VMI image is the projection of the three-dimensional photoelectron momentum distribution onto the two-dimensional (2D) plane, $I(\tau; k_x, k_y)$. In Appendix A, we discuss the subtle difference between the three-dimensional (3D) distribution $I(\tau, k_r, \theta)$ and the 2D projection $I(\tau; k_x, k_y)$. At every pixel representing (k_x, k_y), we fit the modulation of the signal intensity $I(\tau; k_x, k_y)$ by a sum of cosine functions,

$$I(\tau; k_x, k_y) = A + 2B\cos(\omega\tau + C) + 2D\cos(2\omega\tau + E), \tag{3}$$

where A–E are the fitting parameters and all are a function of k_x and k_y. The last term, modulated with a period of 2ω, is added to account for the minor contribution of multiphoton

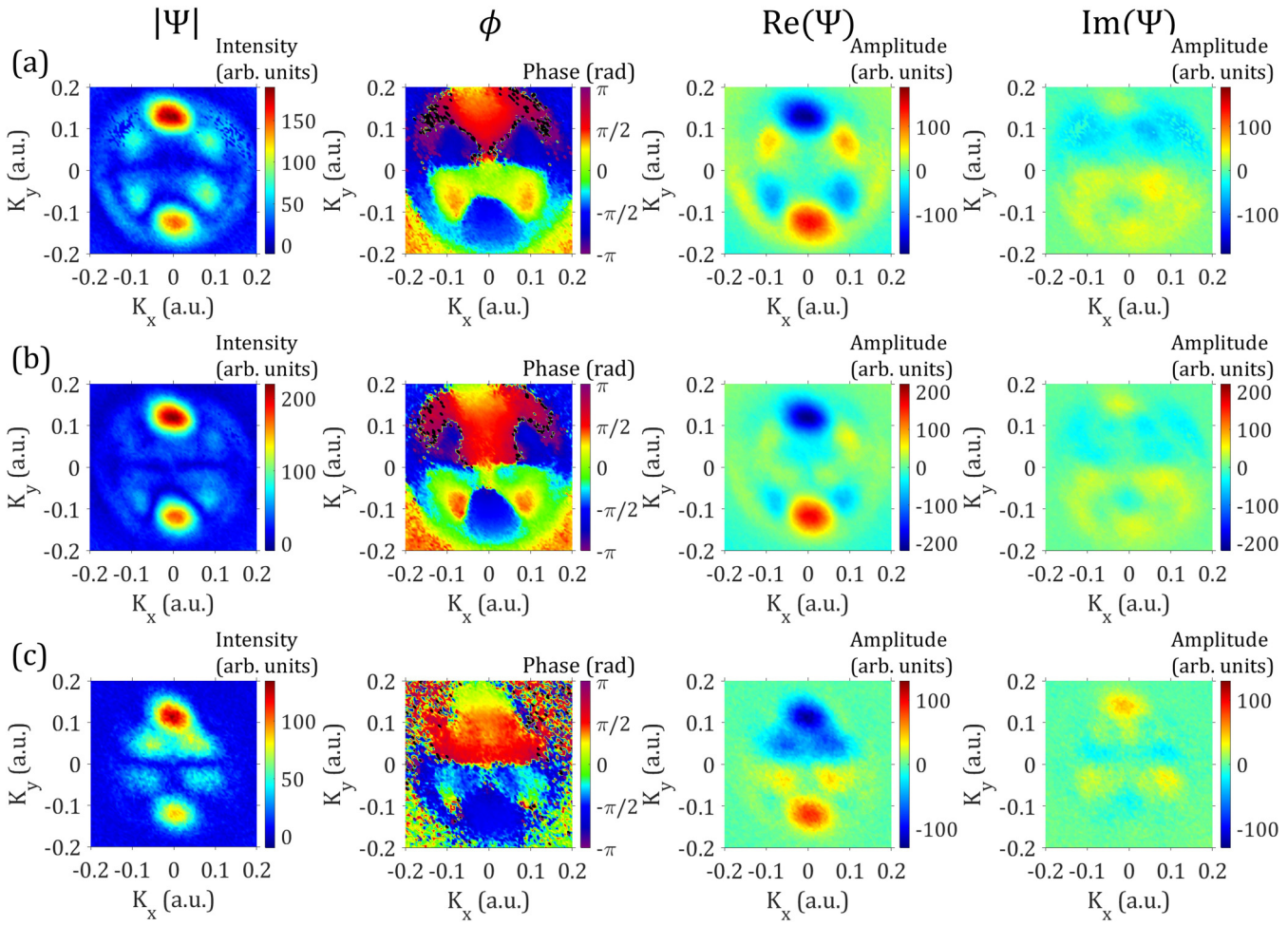

FIG. 4. Measured wave function images. The amplitude and phase distribution $|\Psi(k_x, k_y)|$, $\phi(k_x, k_y)$ and the real and imaginary part of $\Psi(k_x, k_y)$ (columns) for three different experimental conditions [rows (a–c)]. The high-harmonic spectra corresponding to these results are shown in Fig. 3(d). The estimated IR intensity in the VMI is (a) 4.2×10^{12} W/cm^2, (b) 4.6×10^{12} W/cm^2, and (c) 4.5×10^{12} W/cm^2, respectively. The value 0.1 a.u. (atomic units of momentum) corresponds to a kinetic energy of ∼0.13 eV and ∼ 0.19 Å^{-1}.

processes, as described in Appendix B. Comparison of the terms in Eq. (2) with those of Eq. (3) gives

$$A = |\psi_a|^2 + |\psi_b|^2,$$
$$B = |\psi_a||\psi_b|,$$
$$C = (\varphi_a - \varphi_b). \tag{4}$$

We define time zero as when the intensity of the lobe located at 90 ° is maximized. We introduce a "mapping" complex wave function,

$$\Psi(k_x, k_y) \equiv B(k_x, k_y)e^{i\phi(k_x, k_y)},$$
$$\phi(k_x, k_y) = C(k_x, k_y) + a, \tag{5}$$

where a is the arbitrary global phase.

Figure 4 shows the results of the fitting. $|\Psi(k_x, k_y)|$, $\phi(k_x, k_y)$, and the real and imaginary parts of Ψ are plotted for three experimental conditions. From panels (a) to (c), the corresponding high-harmonic spectra are shown as the blue, green, and red curves in Fig. 3(d). For the phase distribution $\phi(k_x, k_y)$, we select $a = \pi/2$ to clarify the phase difference between the upper ($k_y > 0$) and lower ($k_y < 0$) parts. For the real and imaginary parts of the wave function Ψ, we further adjust the arbitrary phase a, so that the magnitude of the sixfold structure in the real part of Fig. 3(a) maximizes. The other fitted distributions, A, D, and E, are present in Appendix B.

In all three cases, a sixfold structure is observed due to the f wave produced by the two-photon ionization [19,20]. In Fig. 4(a), the phase of the neighboring lobes separated by ∼60 ° is shifted by $\sim \pi$. In addition, a ring structure is observed at $k_r \sim 0.18$ a.u. In the real part of Ψ, the amplitude of the sixfold structure has positive and negative values every 60 °. In Fig. 4(b), the sixfold structure is split into two parts in the radial direction and, in total, three features are observed. The outer part of the sixfold structure ($k_r \sim 0.1$ a.u.) has approximately the same phase distribution as the sixfold structure shown in row (a), while the phase of the inner part ($k_r < 0.07$ a.u.) is shifted by $\sim \pi/2$ from the outer part. In Re(Ψ), it is seen that the amplitude oscillates as k_r increases. In Fig. 4(c), the sixfold structure is more enhanced around $k_r \sim 0.07$ a.u. compared with that in row (b). In contrast to the case in row (a), the phase distribution in row (c)

TABLE I. Fitted phase values. The fitted phases of partial waves at the radial momentum $k_r = 0.07$ and 0.11 a.u. for Figs. 6(a) and 6(b), or 0.13 a.u. for Fig. 6(c).

	$K_r = 0.07$ a.u.				$k_r = 0.11$ (or 0.13 a.u.)			
	p	d	f	$\Delta(f-p)$	p	d	f	$\Delta(f-p)$
(a)	4.27	0.55	0.71	–3.56	4.07	0.28	0.43	–3.64
(b)	5.55	1.63	1.49	–4.06	4.11	0.58	0.61	–3.50
(c)	6.44	2.63	2.16	–4.28	5.56	1.53	1.86	–3.70

has approximately a twofold symmetry. The amplitude and phase distributions are resolved with a momentum resolution <0.02 a.u.

C. Decomposition into individual wave functions

We now discuss thedetailed structure of the mapping wave function. To obtain Fig. 4, the fitting was performed at every momentum (k_x, k_y). We convert from Cartesian to spherical coordinates (k_r, θ) in the two-dimensional plane, and fit the signal with radius k_r using spherical harmonics. We expand the wave function $\Psi(k_r, \theta)$ into the product of two individual wave functions, $\psi_a(k_r, \theta)$ and $\psi_b^*(k_r, \theta)$, as follows.

$$\begin{aligned}\Psi(k_r,\ \theta) &= |\psi_a(k_r,\ \theta)||\psi_b(k_r,\ \theta)|e^{i(\varphi_a(k_r,\theta)-\varphi_b(k_r,\theta))}e^{ia}\\ &= |\psi_a(k_r,\ \theta)|e^{i\varphi_a(k_r,\theta)}|\psi_b|e^{-i\varphi_b(k_r,\theta)}e^{ia}\\ &= \psi_a(k_r,\ \theta)\psi_b^*(k_r,\ \theta)e^{ia},\end{aligned} \tag{6}$$

where ψ_b^* is the complex conjugate of ψ_b. ψ_a corresponds to the photoelectron wave function produced by H14, and ψ_b corresponds to that produced by H13 + IR. Each individual wave function is decomposed as

$$\begin{aligned}\psi_a(k_r,\theta) &= A_s(k_r)Y_{00}(\theta) + A_d(k_r)Y_{20}(\theta)e^{i\phi_d(k_r)},\\ \psi_b^*(k_r,\theta) &= A_f(k_r)Y_{30}(\theta)e^{-i\phi_f(k_r)} + A_p(k_r)Y_{10}(\theta)e^{-i\phi_p(k_r)},\end{aligned} \tag{7}$$

where A_i is the amplitude, ϕ_i is the phase for each partial wave, and Y_{ℓ,m_ℓ} are the spherical harmonics which depend only on θ because of the polar symmetry with respect to the polarization axis. The phase of the s wave is set to zero.

At each radial momentum k_r, we fit the angular distribution to obtain the phases and amplitudes of the partial waves by using the following equation,

$$\Psi(\theta; k_r) = P_1(Y_{00} + P_2Y_{20}e^{iP_3})(Y_{30}e^{iP_4} + P_5Y_{10}e^{iP_6}), \tag{8}$$

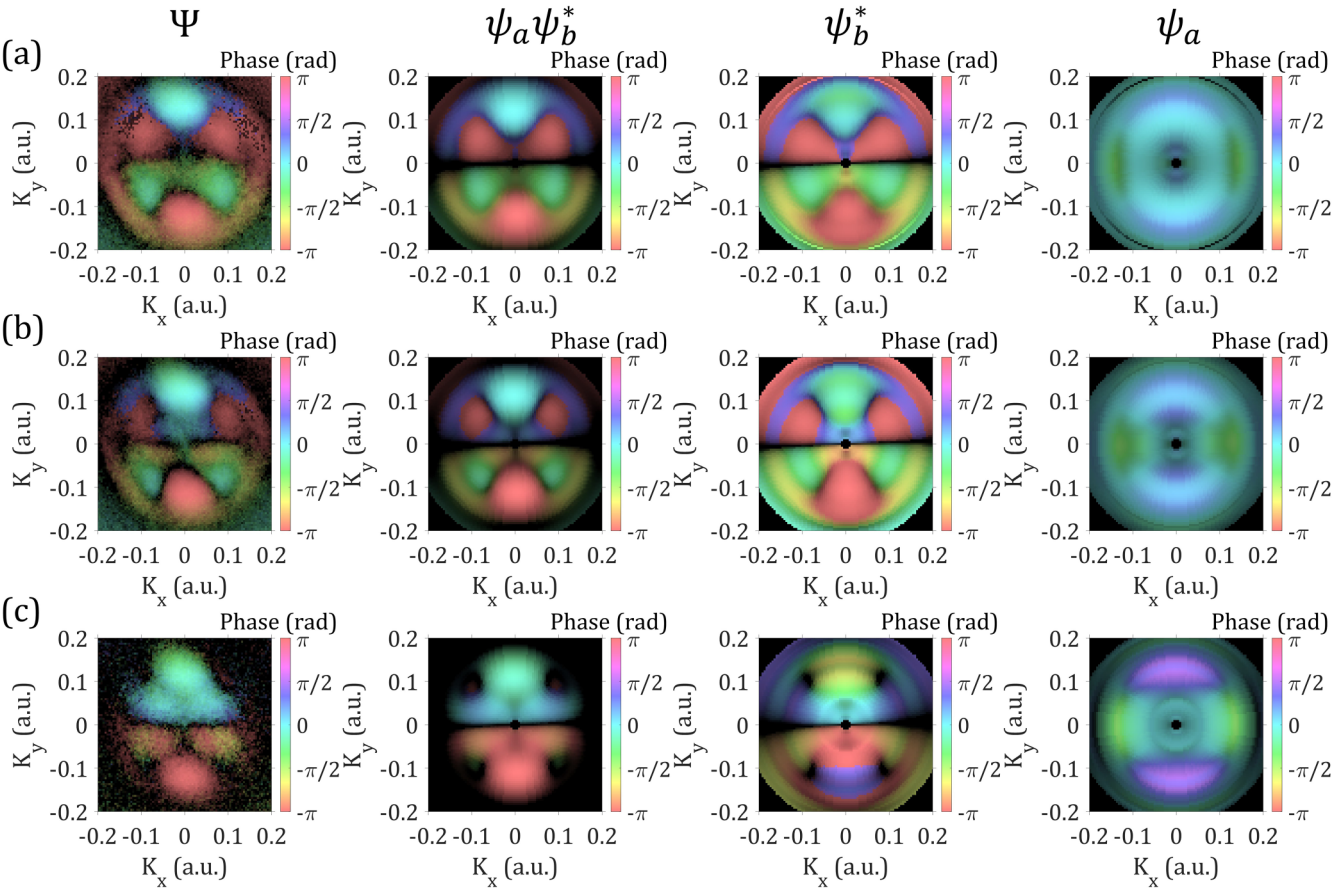

FIG. 5. Decomposed wave function images. Experimentally observed wave function images Ψ (left column), fitted images $\psi_a\psi_b^*$, and disentangled wave functions ψ_b^* and ψ_a for three experimental conditions (a–c). The HSV color space representation is used to display the complex wave functions. The amplitude is given as a color intensity; the phase is given as a color hue. The amplitude is normalized in the range of 0–1 in each figure, and is plotted using a logarithmic scale in the range of $10^{-3.5} - 10^0$. The color bar represents the phase distribution at the maximum amplitude. The two-dimensional color map which represents both phase and amplitude distributions is given in Appendix D. The arbitrary phase a is set to 0. As expected, the fitted images $\psi_a\psi_b^*$ closely resemble the experimentally derived images Ψ.

where P_i are the real fitting parameters, each a function of k_r. P_1 is the product of A_f and A_s. P_2 and P_5 are the amplitudes relative to the s wave and f wave, $P_2 = A_d/A_s$, and $P_5 = A_p/A_f$. In this fitting, one can determine the phase relationship between the p, d, and f waves relative to the s wave, as well as the relative amplitudes, P_2 and P_5. On the other hand, decomposition of P_1 into A_f and A_s is more difficult. Mathematically, the ratio between A_f and A_s may be determined by using the measured angular distribution, while it increases the error of the fitting because of low signal-to-noise ratio in the low-k_r region. Instead, in this study, we assume that the ratio between A_f and A_s is constant over the range of all k_r. In Appendix C, we compare the present analysis with a global fitting method employed in the previous studies [19,20]. We confirm that the phases and the relative amplitudes obtained by Eq. (8) are consistent with the parameters obtained by the global fitting method. Compared to the global fitting method, the present fitting is much faster, allowing us to obtain the full image of the wave function. Using the parameters determined by the fitting with Eq. (8), we reconstruct ψ_a and ψ_b^*, and the product $\psi_a\psi_b^*$.

Figure 5 shows the results of the fitting. We use the HSV (hue, saturation, value) color space to represent the complex wave function, in which the amplitude is represented as the color intensity and the phase is given as the color hue. We set the saturation value to 0.5. We normalize the amplitude in the range of 0–1 for each figure, and plot the logarithmic value in the range of $10^{-3.5} - 10^{0}$ in order to enhance the small amplitudes. As a reference, we also show the same wave functions plotted using the linear scale for the amplitude in Appendix E.

In the left column of Fig. 5, we plot the experimental Ψ to be fitted. This is the same function as shown in Fig. 4, but with the phases and amplitudes plotted in one figure. Using the HSV representation, it is clearly seen that the phases and amplitudes depend on the angle and the radial momentum, and vary with the experimental conditions. The second column shows the reconstructed $\psi_a\psi_b^*$, which is mostly consistent with Ψ for all three conditions. This indicates that Eqs. (7) and (8) are appropriate for disentangling Ψ into the individual components.

The two columns in the right side of Fig. 5 show the disentangled wave functions ψ_a and ψ_b^*. The value of phases ϕ_i, $P_1 = A_sA_f$, and the ratio of the amplitudes between the partial waves, $A_p/(A_p + A_f)$ and $A_d/(A_d + A_s)$, are plotted in Fig. 6. Table I shows the phase values at $k_r = 0.07$ and 0.11 a.u. for Figs. 6(a) and 6(b), and 0.13 a.u. for Fig. 6(c). For all three cases, ψ_b^* is responsible for the sixfold structure as is expected. In Fig. 6(a), ϕ_p and ϕ_f show a small dependence on k_r in the range $k_r < 0.13$ a.u., while in Fig. 6(b), both phases oscillate as k_r decreases. The values of ϕ_p and ϕ_f in Fig. 6(b) change by ~1.4 and ~0.9 rad between $k_r = \sim 0.11$ and ~0.07 a.u. This variation of the phases causes the phase jump which appears in Ψ of Fig. 5(b) at $k_r = \sim 0.07$ a.u. In Fig. 6(c), the three phases increase further from those shown in Fig. 6(b). These phase relationships between the partial waves explain the difference between the threefold and the twofold symmetry in the wave function. At $k_r \sim 0.13$ a.u. in Fig. 6(c), a local minimum is seen in ϕ_p. At this k_r, since the contribution of the p wave is small, the f wave will predominantly interfere with the d and s waves, resulting in the tenfold structure in the interference, as is seen in $\psi_a\psi_b^*$.

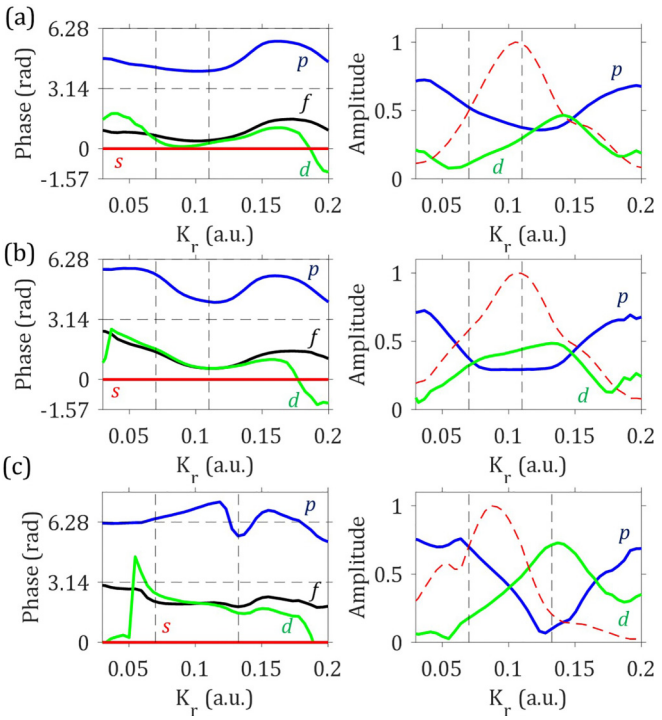

FIG. 6. Fitted phases and amplitudes. (Left) The phase of the f (black), p (blue), d (green), and s waves (red) as a function of k_r for three experimental conditions. (Right) The relative amplitudes for the p wave (blue) and the d wave (green). The definition of the relative amplitude is written in the main text. The red dotted line in the right panel is the normalized curve of $P_1 = A_sA_f$.

So far, we have demonstrated that the phase and amplitude distributions of Ψ can be controlled by changing the XUV photon energy and the IR intensity. Two types of features are observed in Figs. 4 and 5. One is predominantly seen in case (a) in which the neighboring lobes separated by 60 ° have $\sim \pi$ phase difference with approximately threefold symmetry. The other is predominantly seen in case (c) in which the three lobes located at the top and bottom have nearly the same phase values with the twofold symmetry. What is the origin of the variation of the phase distributions? In the presence of the intense IR laser field, the $3d$ Rydberg states of neon are split into two states due to the nearly one IR photon coupling between the $3d$ and $3p$ Rydberg states [22]. The energy level connected to the field-free $3d$ state is responsible for the observed sixfold structure. As the IR intensity increases, the energy of the $3d$ resonant state increases. In our observation, the phase distribution with the twofold symmetry is observed when the H13 photon energy is larger. Thus, the energy levels which produce the twofold symmetry will become important at higher photon energy.

IV. CONCLUSION

Using a two-path interference scheme in the attosecond photoionization of neon atoms, we have recorded the detailed structure of the photoelectron momentum distributions. We have introduced a mapping wave function Ψ which is directly obtained from the photoelectron interferograms by a simple fitting. In contrast to the three-path interference method

[19,20], the phase difference between ψ_a and ψ_b is directly mapped onto Ψ. With this approach, we demonstrate that two types of phase distributions can be switched between threefold and twofold symmetry by changing the experimental conditions. The differences of the phases and amplitudes can be resolved with a momentum resolution of 0.02 a.u. -0.04 Å^{-1} in Ψ. Without assuming cylindrical symmetry, our approach will allow us to measure dynamical changes in narrow momentum ranges of the wave function, for a wide application including molecules.

Furthermore, we disentangle the mapping function Ψ with the partial wave components of the wave functions produced by individual ionization pathways. The calculation of the photoelectron phase at low kinetic energy is challenging, and our results encourage the development of time-dependent Schrödinger equation calculations or analytical models. In order to separate the wave function Ψ into the individual wave functions ψ_a and ψ_b, we have used a linear combination of spherical harmonics. We include s and d waves for ψ_a and f and d waves for ψ_b. In case of other atoms or conditions in which more angular momentum states could be involved, we add the term(s) in Eq. (8) for fitting. In the case of a molecule, instead of using the spherical harmonics, molecular orbitals can be used as a basis set. Combined with a molecular alignment technique [23], it could be possible to image the photoelectron wave function in the ionization continuum in the molecular frame by the method presented here. By comparing theoretical studies [24], the detailed structure of the electron potential or dynamics of electron-electron correlation in a molecule can be studied.

ACKNOWLEDGMENTS

H.N. acknowledges useful discussions with T. Morishita. H.N. acknowledges funding from the Japan Society for the Promotion of Science (JSPS) Grant-in-Aid for Scientific Research (KAKENHI) Grant No. 18H03903, and Waseda University Grant for Special Research Projects 2021N-005. D.M.V. acknowledges funding from the Joint Centre for Extreme Photonics (JCEP).

APPENDIX A: COMPARISON BETWEEN CUT AND PROJECTION IMAGES

The VMI image is a projection of the 3D photoelectron angular distribution onto a 2D plane. Here we have implicitly assumed that a projection of the 3D distribution onto a plane, $I(\tau; k_x, k_y)$, is the same as the radial distribution, $I(\tau, k_r, \theta)$. The usual solution to this problem is to employ an Abel inversion of the VMI data to produce the underlying 3D distribution [25]. Unfortunately in the present case, where the important information is located near the origin, the Abel inversion produces a noisy image. In addition, most Abel inversion techniques assume an up-down symmetry, and use only even order Legendre polynomials. The data here have both even and odd parity, and would require a more sophisticated inversion technique than is usually employed in inverting photoelectron distributions [26]. In Fig. 7, we compare images generated by both approaches, and show that they are reasonably close.

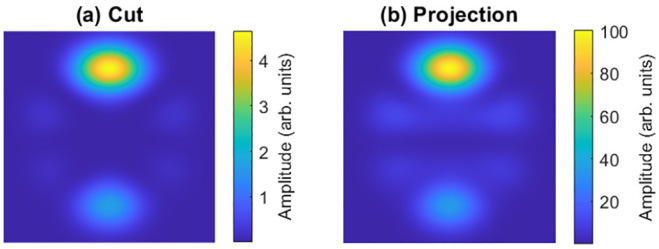

FIG. 7. (a) A cut through the $k_z = 0$ plane of $I(\tau, k_r, \theta)$. (b) A projection of $I(\tau, k_r, \theta)$ onto a plane, equivalent to the VMI image. The images are calculated at a particular delay τ in which the upper and lower lobes have different intensities.

APPENDIX B: FITTED DISTRIBUTIONS FOR DC AND 2ω COMPONENTS

Figure 8 shows A, D, and E defined in Eq. (3) for three experimental conditions, corresponding to the results shown in Figs. 3(a)–3(c) in the main text. We refer to A to as the dc component. The intensity range for D, 2ω component, is set to the same as that of B, ω component, in the main text for comparison. The D component exhibits a sixfold structure in which the radius of k_r is slightly smaller than that of the ω component (see the main text).

The 2ω component D represents the amplitude of the intensity modulation with twice the frequency of the fundamental, IR laser pulse. In the multiphoton ionization process with high harmonics and IR pulses, the harmonic orders separated by 2 are responsible for the 2ω component. In our case, since the spectral intensity of harmonic 15 (H15) is much smaller than H13, and it is less likely that the transition dipole moment of H15 with one IR photon emission (H15- IR) is much larger than that of H13 with one IR photon absorption (H13 + IR), the contribution of the interference between H15–IR and H13 + IR must be negligible. Instead, the interference between H11 + 2 IR and H13 is likely to contribute to the 2ω component, as shown in Fig. 8(d). The photon energy of H11, 17.2 eV, is close to the $3s$ state with a field-free energy of 16.7 eV. The energy of the $3p$ state, 18.7 eV, is also very close to the photon energy of H11 plus one IR photon, H11+IR, 18.8 eV. From the $3p$ state, one IR photon absorption populates the $3d$ state [22]. Since all processes from the ground $2p$ state to the $3d$ state include near-resonant transitions, the pathway of H11 + 2 IR must have a significant transition dipole moment. The other pathway is the direct excitation to the $3d$ state by H13. Since H11 and H13 is separated by 2 IR photons, the interference occurring at the $3d$ level has a 2ω frequency component. An additional one IR photon absorption from the $3d$ level produces the f and p waves in the ionization continuum.

APPENDIX C: COMPARISON WITH THE GLOBAL FITTING AND THE PRESENT FITTING METHOD

In previous experiments [19,20], the amplitude and phase of each photoelectron angular momentum component were determined by a global fitting using a particle-swarm-optimization (PSO) method [27]. We compare the results of the present fitting with the global fitting using an example

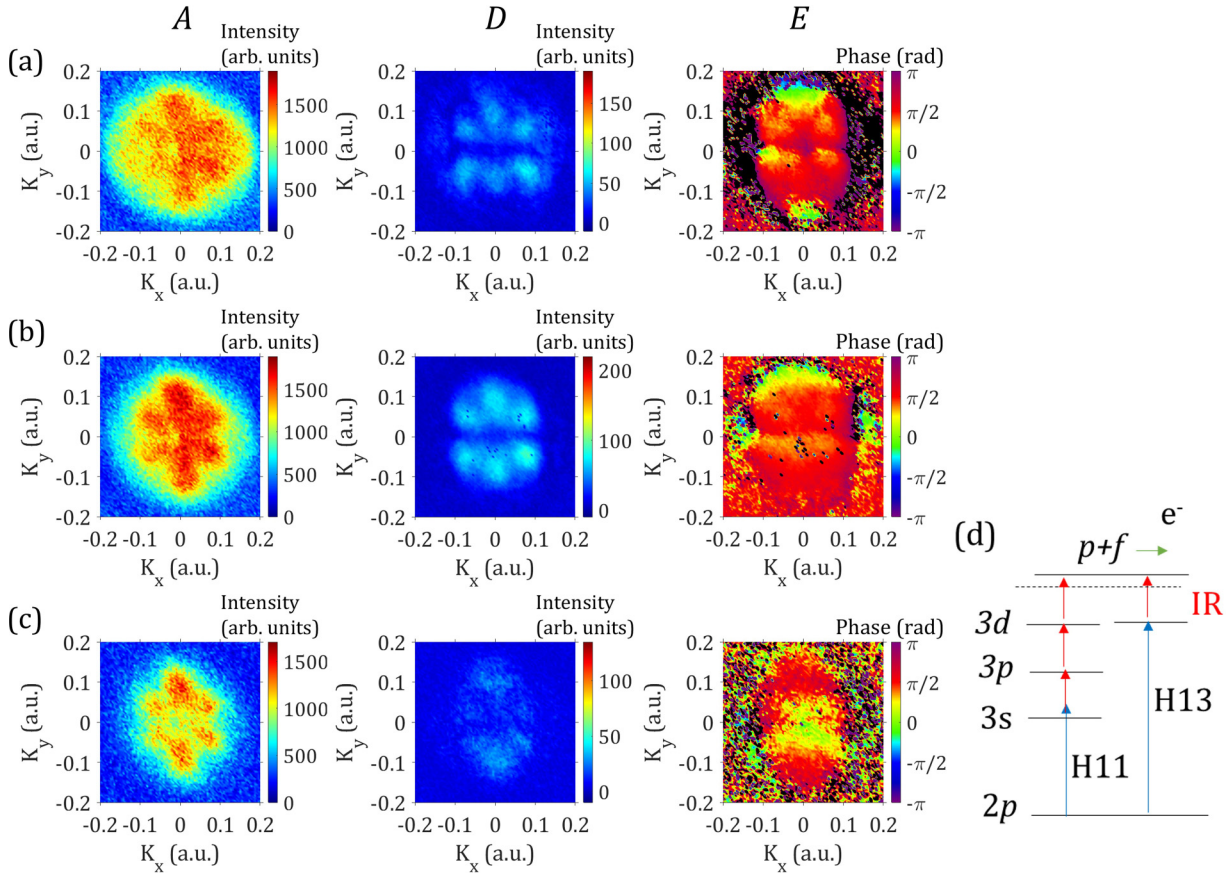

FIG. 8. (a–c) Dc component ($= A$), the amplitude ($= D$) and the phase distribution (E) of the 2ω component for three experimental conditions. (d) Energy diagram for neon and the multiphoton interference scheme.

in which the photoelectron momentum distribution is more structured than that shown in Fig. 4. Figure 9 shows the

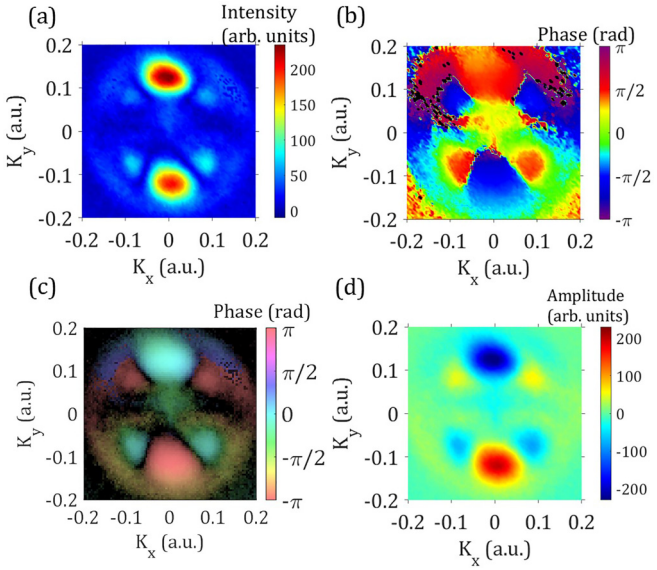

FIG. 9. The measured photoelectron distribution of (a) $|\Psi(k_x, k_y)|$, (b) $\varphi(k_x, k_y)$, (c) the *HSV* representation of $\Psi(k_x, k_y)$, and (d) the real part of $\Psi(k_x, k_y)$. We add the arbitrary phase $a = \pi/2$ for (b). The arbitrary phase for (d) is the same as that in Fig. 4.

measured distributions (a) $|\Psi(k_x, k_y)|$, (b) $\phi(k_x, k_y)$, and (c) the *HSV* representation of $\Psi(k_x, k_y)$ and (d) the real part of $\Psi(k_x, k_y)$ used for the comparison. Figure 10(a) shows the measured angular distribution around the peak of the sixfold structure as a function the XUV-IR delay. We define the XUV-IR delay zero as when the intensity at 90 °, which is the lobe located on the top in Fig. 9, maximizes.

As seen in the main text, the partial wave components are a function of k_r. The global fitting procedure averages over a range of k_r. For the purposes of this comparison, the global fitting considers only k_r in the range 0.06–0.135 a.u.

For the two-path interference model in which the variation with k_r is neglected, the angular distribution as a function of the XUV IR delay τ is given by

$$I(\theta, \tau) = |\psi_a + \psi_b e^{-i\omega\tau}|^2 = |A_s Y_{00} + A_d Y_{20} e^{i\phi_d} + (A_f Y_{30} e^{i\phi_f} + A_p Y_{10} e^{i\phi_p}) e^{-i\omega\tau}|^2, \quad \text{(C1)}$$

where Y_{ℓ,m_ℓ} are the spherical harmonics, A_i is the amplitude, and ϕ_i is the phase for each partial wave. We compare $I(\theta, \tau)$ with that obtained by experiments and determine all parameters.

Figures 10(b) and 10(c) plot $I(\theta, \tau)$ reconstructed by using the parameters obtained by the global fitting and the present fitting. The fitted parameters are summarized in Table II. The ratio of the amplitudes, A_p/A_f and A_d/A_s, and the phases obtained by the global fitting model are consistent with those

TABLE II. The amplitudes and phase of the partial wave components. Note that the amplitudes from the global fitting are normalized to 1, while the amplitudes from the present analysis are not normalized because not all amplitude ratios are known.

			p	d	f	A_p/A_f	A_d/A_s	$\phi_f - \phi_p$	$\phi_d - \phi_s$
Global fitting	Amplitude	0.42	0.36	0.53	0.63	0.57	1.26	—	—
	Phase (rad)	0	3.44	0.17	0.21	—	—	–3.23	0.17
Present analysis	Amplitude	1	0.46	1.23	1	0.46	1.23	—	—
	Phase (rad)	0	3.59	0.38	0.42	—	—	–3.17	0.38

obtained by the present method. The phase difference between $\phi_f - \phi_p$ and $\phi_d - \phi_s$ is also shown in the table.

APPENDIX D: COLOR MAP FOR THE PHASE AND AMPLITUDE DISTRIBUTIONS

Figure 11 shows the two-dimensional color map for plotting the amplitude and phase distributions in Figs. 5 and 12.

APPENDIX E: WAVE FUNCTION IMAGES USING A LINEAR COLOR SCALE

Figure 12 plots the same wave functions as shown in Fig. 5 while using the linear color scale for the amplitude. The amplitude is normalized in the range from 0 to 1 in each figure.

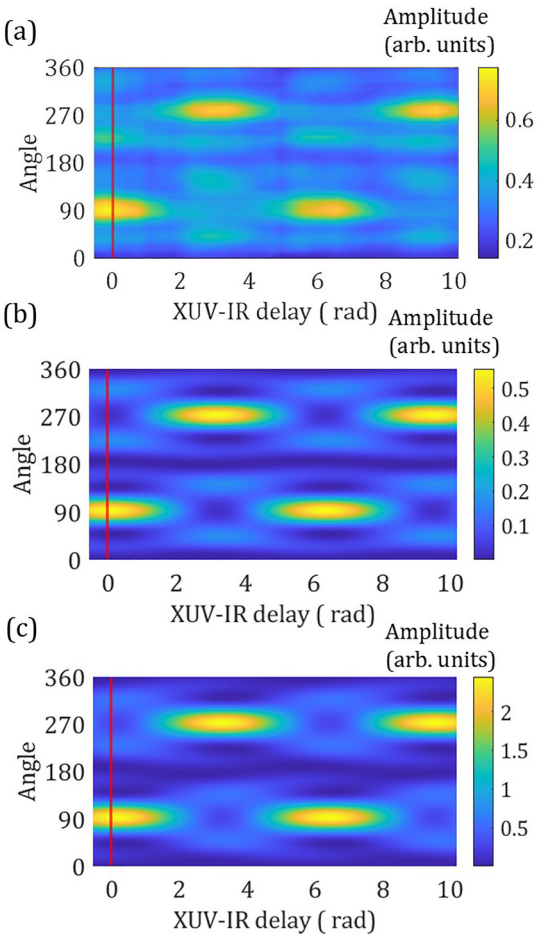

FIG. 10. (a) The experimentally measured photoelectron angular distribution as a function of the XUV IR delay for the sixfold structure of photoelectrons. (b) The result of the global fitting. (c) The result of the present analysis for the same range of k_r. The red line shows the zero delay.

APPENDIX F: THE SPECTRAL PHASE OF HARMONICS

The fitted photoionization phase ϕ_i consists of a sum of the spectral phases of high harmonics, ϕ_H and the atomic phase ϕ_i^a, and thus $\phi_i = \phi_i^a + \phi_H$ [20]. Using the atomic and spectral phases, the mapping wave function is given by

$$\begin{aligned}\Psi &= \left(A_s Y_{00} e^{i(\phi_s^a+\phi_{14})} + A_d Y_{20} e^{i(\phi_d^a+\phi_{14})}\right)\left(A_f Y_{30} e^{-i(\phi_f^a+\phi_{13})}\right. \\ &\quad \left. + A_p Y_{10} e^{-i(\phi_p^a+\phi_{13})}\right) \\ &= \left(A_s Y_{00} + A_d Y_{20} e^{i\phi_d^a}\right)\left(A_f Y_{30} e^{-i\phi_f^a} + A_p Y_{10} e^{-i\phi_p^a}\right) e^{i(\phi_{14}-\phi_{13})} \\ &= A_s A_f \left[Y_{00} + (A_d/A_s) Y_{20} e^{i\phi_d^a}\right] \\ &\quad \times \left[Y_{30} e^{-i[\phi_f^a-(\phi_{14}-\phi_{13})]} + (A_p/A_f) Y_{10} e^{-i[\phi_p^a-(\phi_{14}-\phi_{13})]}\right],\end{aligned} \tag{F1}$$

where ϕ_{14} and ϕ_{13} are the spectral phases of H14 and H13, and the atomic phase of the s wave ϕ_s^a is set to zero. As shown in the main text, we determine the photoionization phases and the relative amplitudes by using the following equation:

$$\Psi(\theta; k_r) = P_1 (Y_{00} + P_2 Y_{20} e^{iP_3})(Y_{30} e^{iP_4} + P_5 Y_{10} e^{iP_6}). \tag{F2}$$

Hence,

$$\begin{aligned} P_3 &= \phi_d^a, \\ P_4 &= -\phi_f^a + (\phi_{14} - \phi_{13}), \\ P_6 &= -\phi_p^a + (\phi_{14} - \phi_{13}). \end{aligned} \tag{F3}$$

Therefore, by subtracting $\phi_{14} - \phi_{13}$ from the fitted phase ϕ_i, the atomic phase is determined. In contrast to previous ex-

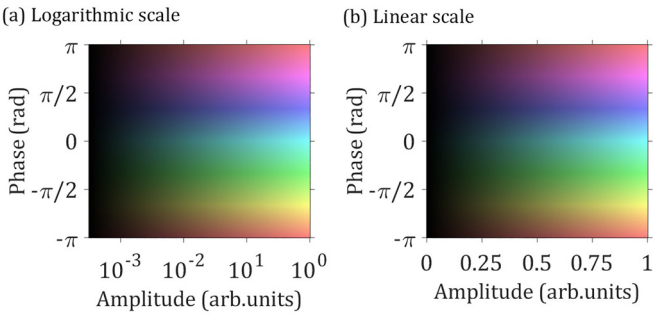

FIG. 11. Two-dimensional color map for the phase and amplitude distributions used in Figs. 5 and 12. The amplitude is plotted in the range of $10^{-3.5} - 10^0$ for the logarithmic scale (a), and 0–1 for the linear scale (b).

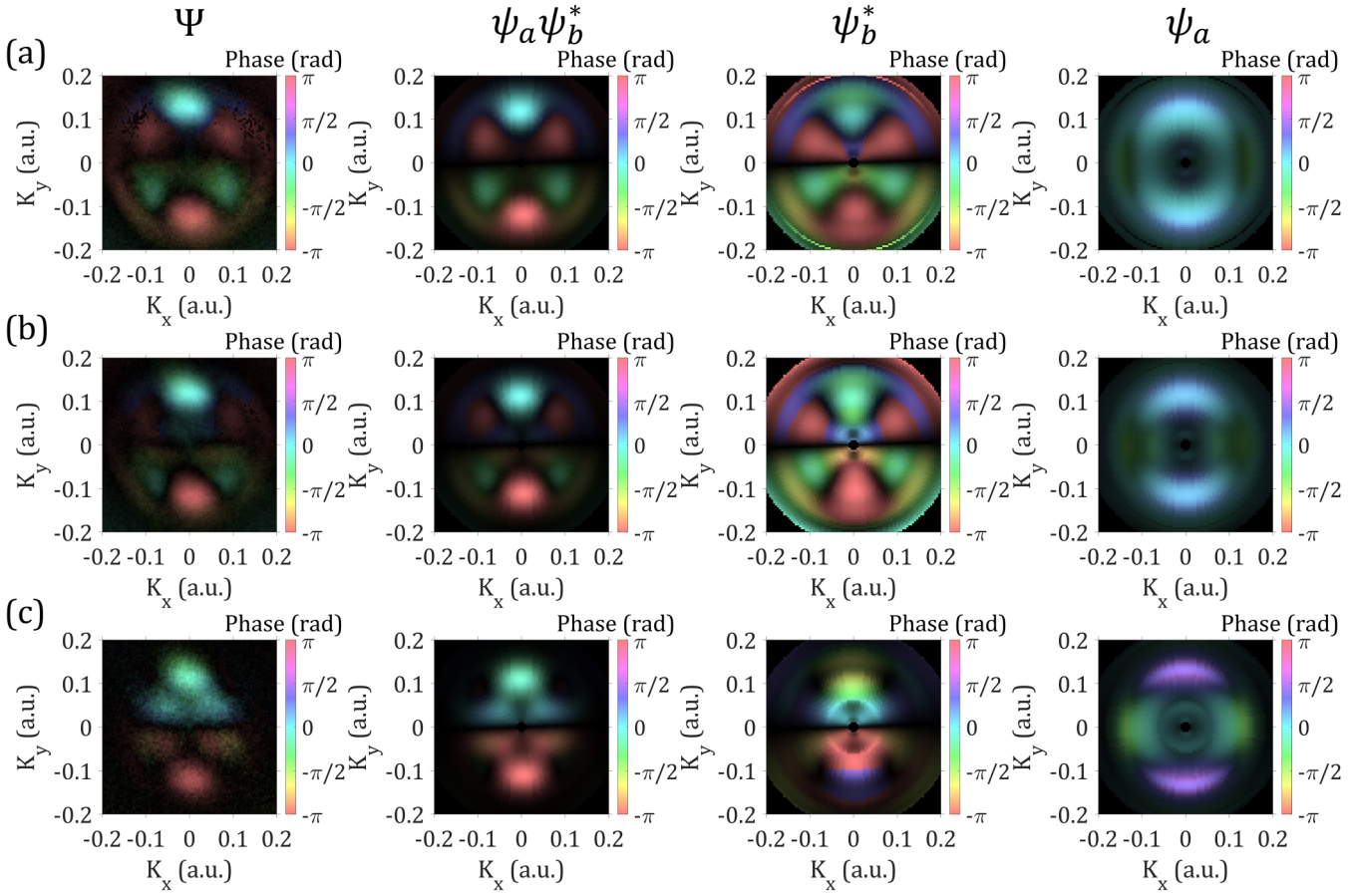

FIG. 12. Same as Fig. 5, except that the color intensity scale is linear instead of logarithmic. The color scale for the phase is the same in both figures.

periments [20], the determination of the spectral phase by the *in situ* method is more challenging, because the 2ω intensity is larger than before. Exact determination of the spectral phase will be the subject of future work.

[1] A. Tonomura, J. Endo, T. Matsuda, and T. Kawasaki, Am. J. Phys. **57**, 117 (1989)]

[2] C. Chen, Y.-Y. Yin, and D. S. Elliott, Phys. Rev. Lett. **64**, 507 (1990).

[3] E. Dupont, P. B. Corkum, H. C. Liu, M. Buchanan, and Z. R. Wasilewski, Phys. Rev. Lett. **74**, 3596 (1995).

[4] F. Krausz and M. Y. Ivanov, Rev. Mod. Phys. **81**, 163 (2009).

[5] M. Hentschel, R. Kienberger, Ch. Spielmann, G. A. Reider, N. Milosevic, T. Brabec, P. Corkum, U. Heinzmann, M. Drescher, and F. Krausz, Nature (London) **414**, 509 (2001).

[6] M. Schultze, M. Fiess, N. Karpowicz, J. Gagnon, M. Korbman, M. Hofstetter, S. Neppl, A. L. Cavalieri, Y. Komninos, Th. Mercouris, C. A. Nicolaides, R. Pazourek, S. Nagele, J. Feist, J. Burgdörfer, A. M. Azzeer, R. Ernstorfer, R. Kienberger, U. Kleineberg, E. Goulielmakis *et al.*, Science **328**, 1658 (2010).

[7] M. Drescher, M. Hentschel, R. Kienberger, M. Uiberacker, V. Yakovlev, A. Scrinzi, Th. Westerwalbesloh, U. Kleineberg, U. Heinzmann, and F. Krausz, Nature (London) **419**, 803 (2002).

[8] H. Niikura, F. Légaré, R. Hasbani, A. D. Bandrauk, M. Yu. Ivanov, D. M. Villeneuve, and P. B. Corkum, Nature (London) **417**, 917 (2002).

[9] J. Itatani, J. Levesque, D. Zeidler, H. Niikura, H. Pépin, J. C. Kieffer, P. B. Corkum, and D. M. Villeneuve, Nature (London) **432**, 867 (2004).

[10] H. Niikura, H. J. Wörner, D. M. Villeneuve, and P. B. Corkum, Phys. Rev. Lett. **107**, 093004 (2011).

[11] M. Meckel, D. Comtois, D. Zeidler, A. Staudte, D. Pavičić, H. C. Bandulet, H. Pépin, J. C. Kieffer, R. Dörner, D. M. Villeneuve, and P. B. Corkum, Science **320**, 1478 (2008).

[12] M. Meckel, A. Staudte, S. Patchkovskii, D. M. Villeneuve, P. B. Corkum, and R. Dörner, Nat. Phys. **10**, 594 (2014).

[13] P. M. Paul, E. S. Toma, P. Breger, G. Mullot, F. Augé, Ph. Balcou, H. G. Muller, and P. Agostini, Science **292**, 1689 (2001).

[14] Y. Mairesse, A. de Bohan, L. J. Frasinski, H. Merdji, L. C. Dinu, P. Monchicour, P. Breger, M. Kovačev, R. Taïeb, B. Carré, H. G. Muller, P. Agostini, and P. Salières, Science **302**, 1540 (2003).

[15] J. M. Dahlström, A. L'Huillier, and A. Maquet, J. Phys. B: At., Mol. Opt. Phys. **45**, 183001 (2012).

[16] C. Ott, A. Kaldun, L. Argenti, P. Raith, K. Meyer, M. Laux, Y. Zhang, A. Blättermann, S. Hagstotz, T. Ding, R. Heck,

J. Madroñero, F. Martín, and T. Pfeifer, Nature (London) **516**, 374 (2014).
[17] C. Liu, Z. Zeng, R. Li, Z. Xu, and M. Nisoli, Phys. Rev. A. **90**, 013403 (2014).
[18] J. Vos, L. Cattaneo, S. Patchkovskii, T. Zimmermann, C. Cirelli, M. Lucchini, A. Kheifets, A. S. Landsman, and U. Keller, Science **360**, 1326 (2018).
[19] D. M. Villeneuve, P. Hockett, M. J. J. Vrakking, and H. Niikura, Science **356**, 1150 (2017).
[20] D. M. Villeneuve, P. Peng, and H. Niikura, Phys. Rev. A **104**, 053526 (2021).
[21] N. Dudovich, O. Smirnova, J. Levesque, Y. Mairesse, M. Yu. Ivanov, D. M. Villeneuve, and P. B. Corkum, Nat. Phys. **2**, 781 (2006).
[22] S. Patchkovskii, M. J. J. Vrakking, D. M. Villeneuve, and H. Niikura, J. Phys. B: At., Mol. Opt. Phys. **53**, 134002 (2020).
[23] P. W. Dooley, I. V. Litvinyuk, K. F. Lee, D. M. Rayner, M. Spanner, D. M. Villeneuve, and P. B. Corkum, Phys. Rev. A **68**, 023406 (2003).
[24] P. Hockett, E. Frumker, D. Villeneuve, and P. Corkum, J. Phys. B: At., Mol. Opt. Phys. **49**, 095602 (2016).
[25] M. J. J. Vrakking, Rev. Sci. Instrum. **72**, 4084 (2001).
[26] G. A. Garcia, L. Nahon, and I. Powis, Rev. Sci. Instrum. **75**, 4989 (2004).
[27] J. Kennedy and R. Eberhart, Particle swarm optimization, in *Proceedings of ICNN'95–International Conference on Neural Networks* (IEEE, New York, 1995), Vol. 4, p. 1942.